## 1.4 Model-based Geometry Reconstruction of Quantum Dots from TEM

*Anieza Maltsi, Thomas Koprucki, Karsten Tabelow, and Timo Streckenbach*

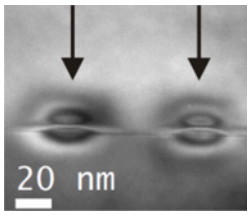


***Fig. 1:*** *TEM image of InAs QDs recorded at TU Berlin showing a coffee-bean-like contrast*

The use of lenses to magnify the vision of objects dates back a couple of centuries. In the early seventeenth century the invention of the microscope really changed the way we may explore tiny objects that are otherwise not accessible to the human eye. Today, many areas of science and technology cannot be thought without different types of microscopes. While the first were based on light in the visible part of the spectrum and thus inherently limited in their spatial resolution due to the connection between the wavelength of the propagating waves and the minimal size of distinguishable objects, modern microscopes use other types of waves to image even tinier objects. One example is *transmission electron microscopy (TEM)* which uses the propagation of electron waves through magnetic lenses to create an image, see [1]. TEM allows imaging of the crystallographic structure of materials down to an atomic scale. As such, TEM has become an indispensable experimental tool to examine objects in life sciences or in material sciences at nanoscales. However, the creation of the image as well as its interpretation inherently require mathematical theory to solve the reconstruction problem for a single specimen and to allow for automated processing of bulks of them.

### Model-based geometry reconstruction

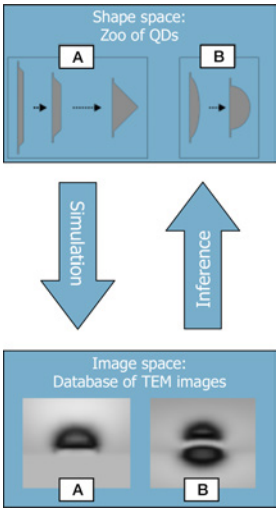


***Fig. 2:*** *From shape space to image space by numerical simulation of TEM images and back by inference on the geometry of a single QD from a given TEM image*

Quantum dots (QD) are semiconductor nanostructures with interesting optoelectronic properties that are determined by their geometry and used in many different fields, such as lasers, quantum cryptography, and quantum metrology. The growth of semiconductor QDs with the desired electronic properties would highly benefit from an assessment of QD geometry, distribution, and strain profile in a feedback loop between epitaxial growth and analysis of their properties. In principle, TEM can be used to assist such an optimization loop of QDs. However, the reconstruction of the geometric properties of QDs from TEM images is a difficult problem due to the limited image resolution (0.5–1nm), the highly nonlinear behavior of the dynamic electron scattering, non-local effects due to strain, and strong stochastic influences resulting from uncertainties in the experiment. In contrast to what is common for images from light microscopy, for TEM imaging of QDs there is no simple one-to-one correspondence between the TEM image, which rather shows the so-called *coffee-bean contrast*, and the shape of the QD, see Figure 1 for an experimental example and Figure 2 for a simulated one.

Within the MATH+ project EF3-1 “Model-based geometry reconstruction from TEM images,” a novel concept was introduced for three-dimensional *model-based geometry reconstruction* (MBGR) of QDs from TEM imaging [2], see Figure 2: MBGR is based on a model for the QD configuration space that includes categorical variables, such as their shape (e.g., pyramidal or lense-shaped) and continuous parameters (e.g., size, height). By the numerical simulation of the imaging process, a database of simulated TEM images spanning the image space for a large number of possible QD configurations and image acquisition parameters can be generated. This simulated image space

can then be assigned to some explicit or implicit metrics and explored by means of statistical methodology, for example, by shape space methods, functional data analysis, or deep learning. Such methods can then be used for inferring the geometry of QDs from experimental TEM images. To realize the idea we combined expertise of the WIAS teams RG 1 *Partial Differential Equations*, RG 3 *Numerical Mathematics and Scientific Computing*, RG 6 *Stochastic Algorithms and Nonparametric Statistics*, and of the *Electron Microscopy and Holography* work group of the *Institut für Optik und Atomare Physik* at Technische Universität Berlin. The work was funded by ECMath (OT7, 06/17–12/18) and MATH+ (EF3-1, 01/19–12/21).

## Darwin–Howie–Whelan equations

For our first step in *model-based geometry reconstruction*, it is necessary to simulate TEM images by numerically solving the equations describing the electron propagation, namely the Darwin–Howie–Whelan (DHW) equations, see [4, Sec. 6.3]. The DHW equations can be derived from the Schrödinger equation

$$\Delta\Psi(\mathbf{r}) + (2\pi|\mathbf{k_0}|)^2\Psi(\mathbf{r}) = -4\pi^2 U(\mathbf{r})\Psi(\mathbf{r}), \tag{1}$$

where $\mathbf{k_0}$ is the wave vector of the monochromatic incoming beam, $\Psi$ is the wave function of the electron beam propagating through the specimen, and $U$ is the reduced electrostatic potential of the crystal, see [1]. For a perfect crystal, the specimen is described by a periodic lattice of atoms $\Lambda \subset \mathbb{R}^3$. We decomposed the spatial variable $\mathbf{r} = (x, y, z)$ into the transversal part $(x, y)$ orthogonal to the thickness variable $z \in [0, z_*]$, see Figure 3.

The column approximation restricts the focus to solutions of (1) that are exactly periodic in $(x, y)$ and are slow modulations in $z$ of a highly-oscillatory function. This is due to the fact that in TEM the beam is formed by fast electrons with high energy, so they will not be scattered very far from the entrance point. Hence, we sought solutions in the form:

$$\Psi(\mathbf{r}) = \sum_{\mathbf{g}\in\Lambda^*} \psi_{\mathbf{g}}(z)\, e^{i\,2\pi\mathbf{k_0}\cdot\mathbf{r}}\, e^{i\,2\pi\mathbf{g}\cdot\mathbf{r}}, \tag{2}$$

where $\Lambda^* \subset \mathbb{R}^3$ denotes the dual lattice, and $\psi_{\mathbf{g}}$ are slowly varying envelope functions. Inserting the multi-beam ansatz (2) into (1), one obtains the DHW equations for infinitely many beams:

$$\frac{\rho_{\mathbf{g}}}{\pi}\frac{\mathrm{d}}{\mathrm{d}z}\psi_{\mathbf{g}}(z) = i\Big(\sigma_{\mathbf{g}}\psi_{\mathbf{g}}(z) + \sum_{\mathbf{h}\in\Lambda^*} U_{\mathbf{g}-\mathbf{h}}\psi_{\mathbf{h}}(z)\Big), \quad \psi_{\mathbf{g}}(0) = \delta_{0,\mathbf{g}}, \quad \text{for } \mathbf{g}\in\Lambda^*, \tag{3}$$

$$\text{where } \rho_{\mathbf{g}} = (\mathbf{k_0}+\mathbf{g})\cdot\nu \text{ and } \sigma_{\mathbf{g}} = |\mathbf{k_0}|^2 - |\mathbf{k_0}+\mathbf{g}|^2,$$

where $\nu = (0, 0, 1)^\top$ is the normal to the crystal surface and where $U_{\mathbf{g}}$ are the Fourier coefficients of the periodic potential $U$. This is an initial value problem for an infinite system of first-order ordinary differential equations describing the propagation of the electron beam through the specimen from $z = 0$ to the exit plane $z = z_*$. The incoming beam ($\mathbf{g} = 0$) is scattered in directions $\mathbf{k_0}+\mathbf{g}$.

One observation here is that the second derivative with respect to $z$ has been dropped. This is due to the high energy of the electrons in the incoming beam. However, the coefficient of the first

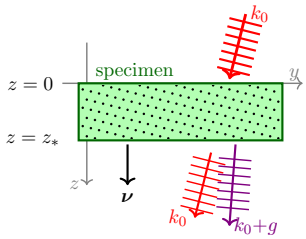


***Fig. 3:*** *The incoming beam with wave vector $\mathbf{k_0}$ enters the specimen, is partially transmitted, and generates beams with nearby wave vectors $\mathbf{k_0}+\mathbf{g}$*

derivative $\rho_{\mathbf{g}}$ can change sign or even become 0 or arbitrarily close to 0 for some $\mathbf{g} \in \Lambda^*$. This means neglecting the second derivative for such $\mathbf{g}$'s makes the DHW equations (for *all* beams $\mathbf{g} \in \Lambda^*$) ill posed. Hence, the DHW equation (3) is only useful for a subset of beams $\mathbf{g}$ where $\rho_{\mathbf{g}}$ is close to $\rho_0 = \mathbf{k_0} \cdot \nu > 0$. The term $\rho_0$ corresponds to the incoming beam ($\mathbf{g} = 0$), which has to be included to satisfy the initial condition $\psi_{\mathbf{g}}(0) = \delta_{0,\mathbf{g}}$. But what do we mean by "close" and how many beams are needed to obtain a reliable approximation for the solution of the Schrödinger equation, in particular for high-energy electron beams?

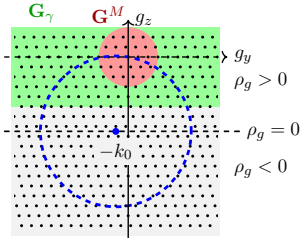


***Fig. 4:*** *Dual lattice $\Lambda^*$ (black dots) and admissible sets $G_\gamma$ (green), $G^M$ (red), and Ewald sphere (blue)*

We approached these questions by systematically investigating the dependence of the solutions $\psi^G = (\psi_{\mathbf{g}})_{\mathbf{g}\in G}$ on the chosen subset $G \subset \Lambda^*$ of the dual lattice. To do this, we first defined the subsets $G$ that make the problem well posed. The condition to be satisfied is $\rho_0 > 0$, so that we can indeed drop the second derivative. For this, we introduced the set $G_\gamma := \{\mathbf{g} \in \Lambda^* \,|\, \rho_{\mathbf{g}} \geq \gamma \rho_0\}$ for $\gamma \in ]0, 1[$, see Figure 4. On this set, the problem is well posed and it also satisfies the initial condition. Next, we defined the appropriate Hilbert space $\mathfrak{H}(G)$ and showed that the reduced DHW system for each $G \subset G_\gamma$ has a unique solution $\psi^G : \mathbb{R} \to \mathfrak{H}(G)$, see [3].

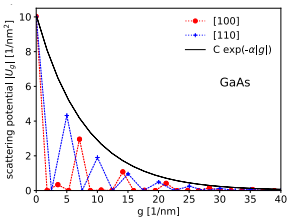


***Fig. 5:*** *Fourier coefficients of the scattering potential for GaAs along different crystallographic directions (red, blue) showing an exponential decay (black)*

The set $G_\gamma$ is still an infinite set. In numerical simulations of TEM images, only a finite number of beams $\mathbf{g}$ near the incoming beam $\mathbf{g} = 0$ is used, such as the two-beam or systematic row approximation, see [1, 2, 4]. We continued our investigation of the dependence of the solutions on finite subsets $G$ of $G_\gamma$. For that purpose, we introduced the set $G^M := \{\mathbf{g} \in \Lambda^* \,|\, |\mathbf{g}| \leq M\}$, for $M > 0$, see Figure 4. This is important because the high-energy electrons are not scattered very far away from the incoming direction. We also assumed that the Fourier coefficients $U_{\mathbf{g}}$ of the scattering potential $\mathcal{U}$ decay exponentially:

$$|U_{\mathbf{g}}| \leq C_{\mathbb{U}}\, \mathrm{e}^{-\alpha_{\mathbb{U}}|\mathbf{g}|} \quad \text{for all } \mathbf{g} \in \Lambda^*. \tag{4}$$

This assumption is satisfied for a wide class of materials, see also Figure 5. Using these assumptions, we proved that the influence of the exact choice of the subsets $G$ such that $G^M \subset G \subset G_\gamma$ is not important if we have enough modes around $\mathbf{g} = 0$. We provided explicit error bounds for the solutions in the finite subsets $G^M \subset G \subset G_\gamma$, which showed an exponential decay in dependence on the radius $M$.

We reduced the set of beams even further by restricting $\mathbf{g}$ into a neighborhood of the Ewald sphere

$$\mathbb{S}_{\mathrm{Ew}} := \{\mathbf{g} \in \mathbb{R}^3 \,|\, |\mathbf{k_0}|^2 - |\mathbf{k_0}+\mathbf{g}|^2 = 0\},$$

see Figure 4. Indeed, in TEM the incoming beam with wave vector $\mathbf{k_0}$ is chosen exactly in such a way that the intersection of the Ewald sphere $\mathbb{S}_{\mathrm{Ew}}$ with the dual lattice $\Lambda^*$ contains, in addition to the incoming beam, a special number of other beams. An example is the so-called *Laue-zone approximation*, which is an approximation of a spherical cap of the Ewald sphere, see Figure 6. By using energy conservation, we provided error bounds for that choice. A similar error analysis was then carried out for both the two-beam and the systematic-row approximation, which are widely employed in TEM image simulation software such as PyTEM [5]. Finally, numerical simulations were done that underpin the quality of the error bounds and thus provide a justification of heuristic beam selection criteria often used in TEM simulation software. For more details on all the above-mentioned results; see [3].

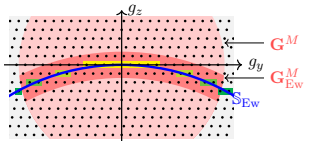


***Fig. 6:*** *Ewald sphere (blue) and Laue zones from the lowest (yellow) to third order (green)*

## Simulation of TEM images of QDs

In semiconductor nanostructures, such as QDs, the dynamical electron scattering as described above for perfect crystals, is additionally influenced by spatial variations in the material composition and by local deformations of the lattice due to elastic strain. In order to model the TEM images, we used elasticity theory to obtain the strain profile and coupled this profile with the DHW equations describing the electron propagation through the sample. We considered QDs composed of InGaAs inside a crystal matrix of GaAs, where the indium content is 80%. The influence of spatial variations in the indium content $c(\mathbf{r})$ and of the lattice deformations given by the displacement field $\mathbf{u}(\mathbf{r})$ can be approximated by the modification of the Fourier coefficients according to

$$U_{\mathbf{g}} \to U'_{\mathbf{g}}(\mathbf{r}) = \left[c(\mathbf{r})U_{\mathbf{g}}^{InAs} + (1 - c(\mathbf{r}))U_{\mathbf{g}}^{GaAs}\right] \times \exp(-2\pi i \mathbf{u}(\mathbf{r}) \cdot \mathbf{g}). \tag{5}$$

The projection of the displacement on the individual reciprocal lattice vector $\mathbf{g}$ enters the coupling as a phase factor. A simulated TEM image is created by propagating the beams through the specimen for every pixel $(x_i, y_j)$, $i, j = 1, \ldots, N$. For the numerical simulation of the TEM images, the elasticity problem is solved with `WIAS-pdelib`, where we took as an input the geometry of the QD and computed the displacement field that enters the DHW-solver PyTEM [5], which computes the TEM image for the chosen excitation. An example of this toolchain for a pyramidal InGaAs QD and the influence of the excitation on the image contrast can be seen in Figure 7. For more details, see [2].

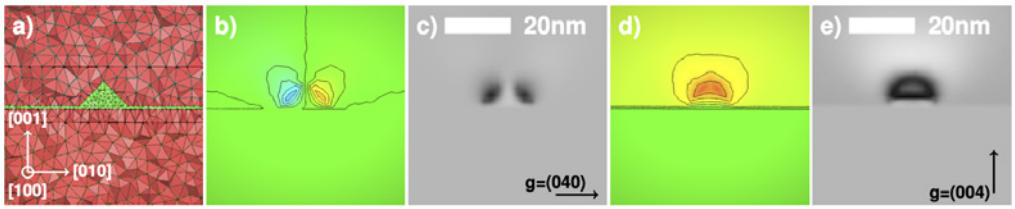


***Fig. 7:*** *Simulation of TEM images: a) QD geometry, b) $u_x$ component, and d) $u_y$ component of displacement field. c) and e): corresponding TEM images for strong beam conditions.*

## Database of TEM images of QDs

Using the toolchain described above, we generated a database of TEM images for initially two classes of geometries: pyramidal and lense-shaped QDs, see Figure 8. This database contains images for different QD geometry parameters (baselength, aspect-ratio, concentration, position) and excitation parameters (acceleration voltage, beam directions). A structured query language (SQL) database is used to store the metadata of the images including the actual values of the parameters, the numerical parameters controlling the solvers, and the file locations. The consistency of parameters and data across the toolchain is ensured by using portable metadata descriptions in JavaScript Object Notation (JSON).

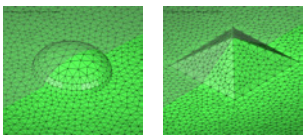

***Fig. 8:*** *Three-dimensional geometry for lense-shaped and pyramidal QD*

Examples from the database are shown in Figure 9, where we have the TEM images for four geometries (flat and full lense-shaped, full and truncated pyramid) for two different excitations. An interesting first observation with the human eye by comparison with experimental data is that the

QD is lense shaped, while before it was considered to be a pyramidal one. For better and automated classification of QDs, we need methods like deep learning, which is an ongoing work in our project.

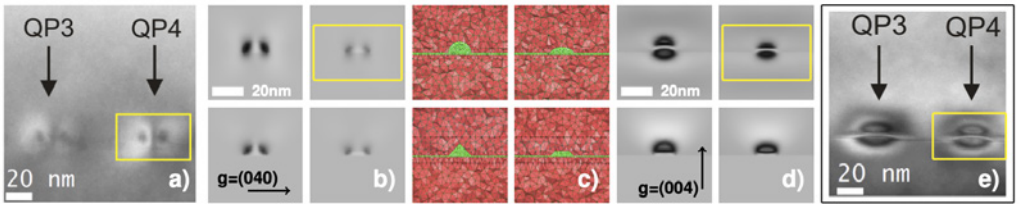


***Fig. 9:*** *Comparison of experimental (a) and e)) and simulated (b) and d)) TEM images for geometries shown in c)*

## Conclusions and outlook

We studied the mathematical structure of the DHW equations that led to a justification of heuristic beam selection criteria and explicit error bounds for different cases, including the widely used two-beam and systematic-row approximation, see [3]. The analysis is currently extended to the impact of strain in the system, which led to a mathematical underpinning of symmetries observed in TEM images; see, e.g., [6].

Together with Tore Niermann from Technische Universität Berlin, we developed a software for the simulation of TEM images for semiconductor QDs. Our toolchain was also applied to more general strained semiconductor nanostructures, as, for example, in [6] for quantum wells in tilted TEM lamellas. With this toolchain, we simulated a database of TEM images for different configurations, which will now be used for our last step in model-based geometry reconstruction, namely the classification of QDs and the analysis of the image space via methods like deep learning.

## References

[1] M. De Graef, *Introduction to conventional transmission electron microscopy*, Cambridge University Press, 2003, DOI 10.1017/CBO9780511615092.

[2] A. Maltsi, T. Niermann, T. Streckenbach, K. Tabelow, T. Koprucki, *Numerical simulation of TEM images for In(Ga)As/GaAs quantum dots with various shapes*, Opt. Quantum Electron., **52** (2020), pp. 257/1–257/11, DOI 10.1007/s11082-020-02356-y.

[3] T. Koprucki, A. Maltsi, A. Mielke, *On the Darwin–Howie–Whelan equations for the scattering of fast electrons described by the Schrödinger equation*, SIAM J. Appl. Math., **81**:4 (2021), pp. 1551–1578, DOI 10.1137/21M139164X.

[4] E.J. Kirkland, *Advanced Computing in Electron Microscopy*, Springer, 3rd ed., 2010, DOI 10.1007/978-1-4419-6533-2.

[5] T. Niermann, *PyTEM: A Python-based TEM image simulation toolkit. Version 3.0.9. [Software]*, Technische Universität Berlin, 2019.

[6] L. Niermann, *Untersuchung und Anwendung der dynamischen Beugung an inhomogenen Verschiebungsfeldern in Elektronenstrahlrichtung in Halbleiterheterostrukturen*, Doctoral Thesis, Technische Universität Berlin, 2021, DOI 10.14279/depositonce-11310.